IEEE Access
Multidisciplinary ⋮ Rapid Review ⋮ Open Access Journal

Received 18 February 2025, accepted 26 March 2025. Date of publication 00 xxxx 0000, date of current version 00 xxxx 0000.

Digital Object Identifier 10.1109/ACCESS.2025.3557085

Compound Mask for Divergent Wave Imaging in Medical Ultrasound

ZAHRAA ALZEIN[1,2], **MARCO CROCCO**[2], **AND DANIELE D. CAVIGLIA**[1], **(Life Member, IEEE)**
[1]Dipartimento di Ingegneria Navale, Elettrica, Elettronica e delle Telecomunicazioni (DITEN), Università degli Studi di Genova, 16126 Genova, Italy
[2]Esaote S.p.A, 16153 Genova, Italy

Corresponding author: Zahraa Alzein (zahraa.alzein@edu.unige.it)

ABSTRACT Divergent wave imaging with coherent compounding allows obtaining broad field-of-view and higher frame rate with respect to line-by-line insonification. However, the spatial and contrast resolution crucially depends on the weights applied in the compound phase, whose optimization is often cumbersome and based on trial and error. This study addresses these limitations by introducing a closed-form approach that maps the transmit apodization weights used in synthetic aperture imaging into the compound mask applied to divergent wave imaging. The approach draws inspiration from a successful technique developed for plane wave imaging, leveraging synthetic aperture imaging as a reference due to its superior image quality. Unlike the previous work on plane waves, the proposed approach is not limited to linear probe geometries but works seamlessly also with convex ones, thus expanding the scope of applicability of divergent wave imaging. Moreover, it handles arbitrary spatial arrangements of virtual sources generating divergent waves. The approach has been validated through simulated data using both linear and convex probes, demonstrating that the Full Width at Half Maximum (FWHM) in Divergent Wave Linear Array (DWLA) increased by 7.5% at 20 mm and 9% at 30 mm compared to Synthetic Aperture Linear Array (SALA). For Divergent Wave Convex Array (DWCA), the increase was 1.64% at 20 mm and 26.56% at 30 mm compared to Synthetic Aperture Convex Array (SACA), witnessing the method's effectiveness.

INDEX TERMS Compound mask, divergent wave imaging, synthetic aperture imaging, transmit apodization.

I. INTRODUCTION

Divergent wave imaging (DWI) is an advanced ultrafast ultrasound technique that enables broad field of view and a higher frame rate with respect to traditional focused transmission and line-by-line reconstruction [1], [2]. By generating spherical wavefronts from virtual sources, DWI achieves wide coverage in a single transmission, making it particularly suitable for dynamic imaging applications such as cardiac and abdominal ultrasound [3]. The high frame rates offered by DWI allow for real-time visualization of fast-moving structures, such as heart valves and blood flow [4], [5]. However, the high frame rate is accompanied by low quality in terms of resolution and contrast because the beamforming process is applied only in the receive mode. This problem can be mitigated by using coherent recombination of echoes related to several divergent-wave transmissions, to recover high-quality images without degrading the high-frame-rate capabilities, as previously proposed for plane wave imaging. This method, originally detailed by Montaldo et al. [6] for plane waves, leverages the coherent summation of echoes from various plane wave transmission angles. The compound method can be extended to divergent waves, by substituting the transmission angles with the positions of the virtual source from which the divergent waves are assumed to originate. A crucial step in coherent compounding is the optimization of the compounded weights, or compound mask, i.e. the weights multiplied by each component before the coherent sum. The compound mask in DWI functions similarly to transmit apodization in conventional ultrasound. However, instead of applying apodization weights to the transmitted signals, the compound mask weights are applied to the beamformed signal in reception, related to each point in the imaging grid.

The associate editor coordinating the review of this manuscript and approving it for publication was Binit Lukose.

© 2025 The Authors. This work is licensed under a Creative Commons Attribution 4.0 License.
For more information, see https://creativecommons.org/licenses/by/4.0/

A. RELATED WORK

In conventional ultrasound with focused transmission, apodization is applied by varying the amplitude of transmitted signals across the transducer elements, shaping the transmitted beam profile to minimize acoustic energy in off-axis directions. First studies investigated the relationship between predefined apodization windows, like Hamming, Hann, Blackman, Tukey etc. with the resulting beam pattern shape, extending the well known findings of the narrowband case to the wideband one employed in most of the medical ultrasound modalities [7]. Similar approaches have been applied in the reception phase, dynamically varying the apodization with the time of arrival of the echoes [8], [9]. Besides predefined windows, apodization weights have been synthesized through cost function minimization, aimed at optimizing trade-off between side lobe level and main lobe width. Among them, approaches based on least squares [10]or stochastic methods [11]. Another approach derives sub-optimal apodization for each focal depth through nonlinear transformation of a baseline window related to a reference depth [12]. Recent advancements have introduced adaptive apodization techniques, such as minimum variance beamforming, which dynamically adjust weights based on received data to further enhance image quality [13]. However, these methods often require iterative optimization, increasing computational complexity and limiting real-time applicability. To cope with this limitations other adaptive approaches select or combine a limited set predefined apodization windows based on the real time analysis of received data [14], [15], thus reducing the number of variables involved and the computation time.

Since focused transmission achieves optimal focusing just at one fixed depth, unfocused tranmit methods have been explored to overcome this limitation. A reference unfocused method is the so called Synthetic Transmit Aperture Imaging (STAI) [16], in which every probe element transmits in sequence and the received signals related to each transmission are aligned and compounded together to beamform every image point. Transmit apodization in STAI is applied in the compounding step of the reception phase: in this way it can be dinamically taylored to each focal depth. STAI transmit apodization can be set borrowing from methods developed for focused tranmission, just setting independently the apodization window for each focal depth. Though STAI achieves theoretically optimal beam pattern it suffers from poor SNR due to limited amount of energy transmit by each element. Moreover the frame rate remains comparable to the one of focused tranmissions.

To overcome these limitations other unfocused transmission methods, based on the generation of coherent plane waves (PWs) [17] and divergent waves (DWs) [1], [2], have been developed, making it possible to achieve ultrafast imaging with high frame rates and wide fields of view. As for STAI, receive signals related to different tranmissions are compounded together. However, differently from STAI, the computation of optimal compound weights has not a straightforward relation with transmit anodization, and it is subject of ongoing research. For PWs some studies have drawn parallels between coherent plane-wave compounding (CPWC) and STAI, suggesting that STAI apodization techniques can be adapted for angular weights in CPWC [18]. Other approaches aim to dynamically estimate the compound weights from the received data, for example adopting Capon's minimum variance beamforming [19]. Recent advancements have incorporated Independent Component Analysis (ICA) into CPWC for angular apodization. ICA decomposes the received signals into statistically independent components, which helps estimate the angular weights more effectively [20]. This method assumes that each plane-wave transmission provides a non-independent observation of the target field, thus enabling the reconstruction of high-quality images through optimal weight estimation.

These adaptive approaches have not yet been investigated for DWI. Various researchers have proposed different compounding strategies for DWI [21]. Two predominant transmit sequences for coherent compounding have been described thus far. One method involves generating a divergent wave using the full aperture, whereby the point spread function (PSF) is rotated between transmits by moving the virtual focus point along an arc at a constant distance from the probe's center [1], [2]. The other method uses only part of the aperture to generate the divergent wave, tilting the PSF by sliding the active aperture across the array [22]. It remains uncertain which of these methods yields superior results. According to [21], spatial compounding by shifting the active aperture of a diverging wave source can enhance image quality more effectively than rotating a diverging wave generated with the full aperture. However, this study does not address how to apply transmit apodization in DWI or what the optimal weights to apply during coherent compounding are. A summary of related works on apodization strategies, coherent compounding techniques, and compound mask optimization is presented in Table 1. The table systematically compares prior studies based on their methodologies, key contributions, and limitations.

B. RESEARCH GAP AND CONTRIBUTIONS

While prior research has advanced the understanding of apodization in synthetic aperture imaging and coherent compounding in plane wave imaging, the optimization of compound weights for divergent wave imaging remains an open challenge. Existing methods either rely on empirical weight assignment or computationally intensive adaptive algorithms, limiting their practicality in real-time applications. This work addresses this gap by deriving a relationship between an arbitrary apodization law in STAI and the compound mask weights in DWI, thus leveraging established optimization criteria in STAI transmit apodization. In particular, under suitable hypotheses, a closed-form solution is computed allowing straightforward mapping of STAI apodization

TABLE 1. Analysis of different approaches for key update on apodization and compound mask optimization.

Study	Methodology	Key Contributions	Limitations
Seo and Yen [14]	Dual apodization with cross-correlation (DAX)	Proposed a sidelobe suppression method by combining two apodized images	Not applicable to coherent compounding in ultrafast imaging
Thoen [7]	Aperture apodization using standard weighting functions (Hamming, Hanning, Blackman)	Defined classical windowing techniques for focused beamforming	Not designed for ultrafast imaging, no coherent compounding
Guenther and Walker [10]	Optimal apodization using constrained least squares	Reduced sidelobe levels via optimal weight selection for medical ultrasound	Requires high computational resources, not real-time applicable
Synnevag et al. [13]	Adaptive beamforming for medical ultrasound	Introduced data-dependent apodization to enhance resolution adaptively	High computational complexity, limited real-time feasibility
Montaldo et al. [6]	Coherent Plane-Wave Compounding (CPWC) for high-frame-rate imaging	Established angular coherent compounding for plane wave imaging	Did not consider apodization weight transfer from SAI to DWI
Rodriguez-Molares et al. [18]	Angular apodization for CPWC	Adapted synthetic transmit aperture imaging (STAI) apodization to CPWC weights	Only applicable to plane-wave imaging, no extension to DWI
Komini et al. [21]	Spatial compounding techniques for DWI	Evaluated two different methods for generating divergent waves in compounding	Did not address transmit apodization or optimal weight selection
Goudarzi et al. [20]	Independent Component Analysis (ICA) for angular apodization	Proposed a method to estimate angular weights for CPWC using ICA	Focused only on plane-wave imaging, not applicable to DWI
This work	Closed-form mapping of synthetic aperture apodization to DWI compound mask	Provides a direct and systematic method for transferring optimized SAI apodization weights into DWI compounding weights, avoiding empirical tuning	Ensures real-time feasibility and applies to both linear and convex arrays

coefficients into DWI compound mask coefficients. The method works for both linear and convex probe geometries and arbitrary arrangements of virtual source positions, thus allowing the approach to be widely applicable. In silico tests confirm the good agreement between STAI and DWI images once the mapping method is applied.

The contributions of this study can be summarized as follows:

- Derivation of a closed-form approach to compute compound mask weights for divergent wave imaging (DWI), enabling direct mapping from transmit apodization weights used in synthetic aperture imaging (SAI). This method eliminates the need for complex and computationally intensive optimization algorithms.
- The proposed approach significantly enhances the spatial and contrast resolution in DWI by optimizing the compound mask weights applied during coherent compounding. This optimization reduces the dependence on trial-and-error methods, offering a systematic solution.
- The method is adaptable for both linear and convex probe geometries, supporting various spatial arrangements of virtual sources. This broadens the scope of application, making the method suitable for a range of high-frame-rate ultrasound imaging scenarios.
- The compound mask weights can be computed offline, minimizing the computational load during real-time imaging. This reduces memory requirements and computational overhead compared to traditional apodization techniques.
- Validation is performed using simulated data for both linear and convex geometries. Results demonstrate the approach's effectiveness in preserving lateral resolution, closely matching the performance of synthetic aperture imaging (SAI) apodization.

The paper is organized as follows. In Section II, the theoretical derivation of the compound mask function for divergent wave imaging (DWI) is presented, along with its relationship to synthetic aperture imaging (SAI) transmit apodization. Section III presents the results and discussion, which includes the simulation setup, parameters used for validation, and a detailed analysis of the results obtained. Section IV discusses the limitations of the study and outlines potential avenues for further optimization and experimental validation. Finally, Section V concludes with a summary of the key findings and contributions of the study, as well as future research directions.

II. MATERIALS AND METHODS

A. SYNTHETIC APERTURE IMAGING (SA) WITH LINEAR AND CONVEX PROBES

Synthetic Aperture Imaging (SA) is used in ultrasound imaging to combine signals from multiple transmit-receive events to form a high-resolution image. SA allows for dynamic focusing in transmission and reception and improves image quality and resolution. The signal reconstructed at any point (x,z) in the imaging field can be mathematically represented by the following equation:

$$S_{SA}(x,z) = \sum_{r=1}^{M} u_r(x,z) \sum_{t=1}^{N} v_t(x,z) h_{tr}\left(\frac{D_t}{c_0} + \frac{D_r}{c_0}\right) \quad (1)$$

where $u_r(x,z)$ and $v_t(x,z)$ are the receive and transmit apodization windows function element index r and t and image point coordinates x, z. The transmit apodization $v_t(x,z)$ is the weight applied to the signal transmitted by element t.[1] The receive apodization $u_r(x,z)$ is the weight applied to the signal received by the element r. The indices M and N are the number of active transmit and receive elements, respectively. h_{tr} is the two-way impulse response from transmit element t to receive element r; D_t and D_r are the distances between the point (x,z) and elements t and r, whose coordinates are x_t, z_t and x_r, z_r respectively, and c_0 is the medium's sound speed. The representations for both synthetic aperture with linear array (SALA) and convex array (SACA) are shown in Figure 1.

B. DIVERGENT WAVE IMAGING

A standard approach to generate divergent waves is to consider a virtual source point i, of coordinates (x_i, z_i) and compute the relative arrival times of a spherical wave propagating from the virtual source to each active probe element location. These relative times of arrival are then applied as a transmission delay curve to the probe elements to generate a divergent field approximating the spherical one in the image plane. The effect of angular compounding, achieved in plane wave transmission by steering the plane wave angle is achieved here by moving the virtual source in different locations. The optimal placement of virtual sources is a subject of ongoing research but it is outside of the scope of this paper. Given a set of virtual source positions, the signal reconstructed at every point (x,z) can be expressed as follows:

$$S_{DW}(x,z) = \sum_{r=1}^{M} u_r(x,z) \sum_{i=1}^{V} w_i(x,z) \hat{h}_{ir}\left(\frac{D_i}{c_0} + \frac{D_r}{c_0}\right) \tag{2}$$

where $w_i(x,z)$ denotes the compound mask function of virtual source index i and image point coordinates. The compound mask is defined as the set of weights applied to the beamformed data related to a specific virtual source in transmission, at each image point (x,z) [23]. $\hat{h}_{ir}$ is the two-way impulse response of the divergent wave from the virtual source i to the image point (x,y) and back to the receive element r, and D_i is the distance between the virtual source of coordinates (x_i, z_i) and the image point. The impulse response of the divergent wave field can be described as a linear combination of impulse responses related to each active probe element in transmission with proper relative delays:

$$\hat{h}(t)_{ir} = \sum_{t=1}^{N} h_{tr}(t - D_{it}/c_0) \tag{3}$$

where D_{it} is the distance between the virtual source i and the transmit element t. Substituting the above expression into the equation for the diverging wave imaging one obtains:

$$S_{DW}(x,z) = \sum_{r=1}^{M} u_r(x,z) \sum_{i=1}^{V} \sum_{t=1}^{N} w_i(x,z) h_{tr}\left(\frac{D_t}{c_0} + \frac{D_r}{c_0} + \tau_{it}\right) \tag{4}$$

where τ_{it} is given by:

$$\tau_{it} = (D_i - D_t - D_{it})/c_0 \tag{5}$$

In Figure 2 the respective distances D_i, D_r,D_{it} are displayed with the linear and convex probe geometries. From the above expression, it can be noticed that both $S_{SA}(x,z)$ and $S_{DW}(x,z)$ can be thought as a linear combination of two-way probe elements impulse responses $h_{tr}(t)$. This allows, under opportune hypotheses, to derive a simple relationship between the compound mask of S_{DW} and apodization weights of S_{DW}, as described in the next Section.

C. RELATION BETWEEN TRANSMIT APODIZATION IN STAI AND COMPOUND MASK IN DWI

In the work of Rodriguez-Molares et al. [18], the authors derived a relationship between apodization in STAI and CPWC, showing that under certain conditions, the angular compounding weights can be derived in closed form from the transmit apodization window of STAI. Here we adapt their approach to divergent waves generated by virtual sources and arbitrary probe geometries. First of all, under the same assumptions of [18] a linear relationship between the compound mask for divergent waves and transmit apodization can be derived assuming that the last expression of $S_{DW}(x,z)$ and the expression for $S_{SA}(x,z)$ are equivalent. The following expression yields:

$$\sum_{i=1}^{V} w_i(x,z) H(i,t) = v_t(x,z) \tag{6}$$

where

$$H(i,t) = \frac{E(\tau_{it})}{E(0)} \tag{7}$$

where $E(t)$ is the convolution of the transmit pulse with the two-way electroacoustic transfer function of the probe elements (see Eq. 14 in [18]). Collecting the above equations for each apodization weight $v_t(x,z)$ a linear system is derived from which the compound mask can be computed, as described in [18]. If we display the matrix $H(i,t)$ in Figure 3, we can see that only a few elements, corresponding to values of τ_{it} close to zero, are different from zero. This means that under the additional hypothesis of short-time transmitted pulse, already introduced in [18], it is possible to approximate the matrix $H(i,t)$ in Eq. 6 as diagonal with non-zero values equal to 1. As a consequence, the only non-zero contribution of the sum of Eq. 6 is the one for which $\tau_{it} = 0$. In other words Eq. 6 becomes $w_i(x,z) = v_t(x,z)$ for the couple of (i,t) fulfilling the condition $\tau_{it} = 0$. Looking at the definition of τ_{it} we see that it represents the difference between the distance from the virtual source

---

[1] Notice that in SA imaging transmit apodization is actually applied to the received signal. This is mandatory to make it a function of imaging point (x,z).

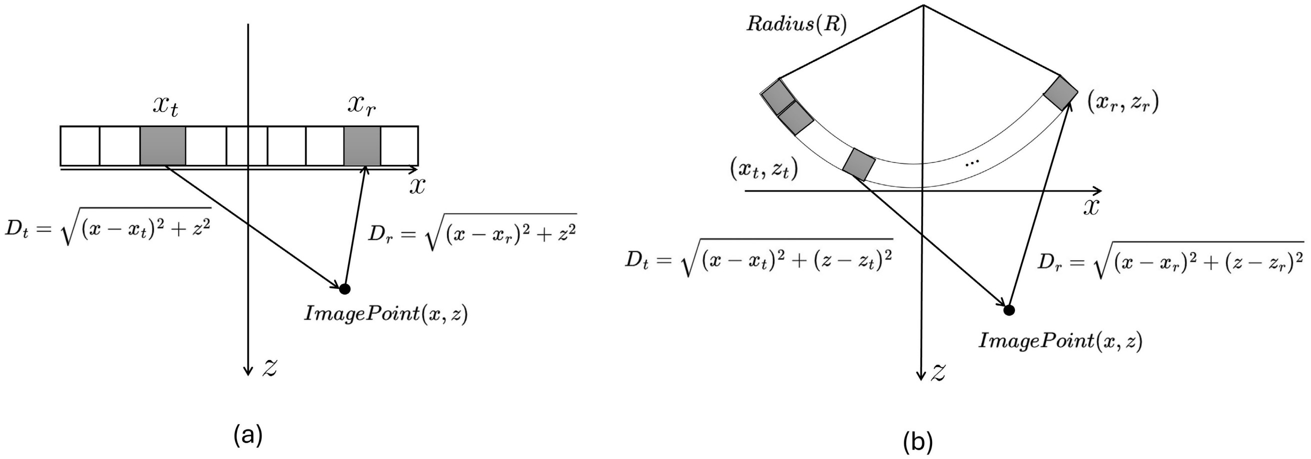

FIGURE 1. **Comparison of SA Linear and Convex Probe Configurations with distances between image point (x, z) and probe elements coordinates in transmission (x_t, z_t) and reception (x_r, z_r).**

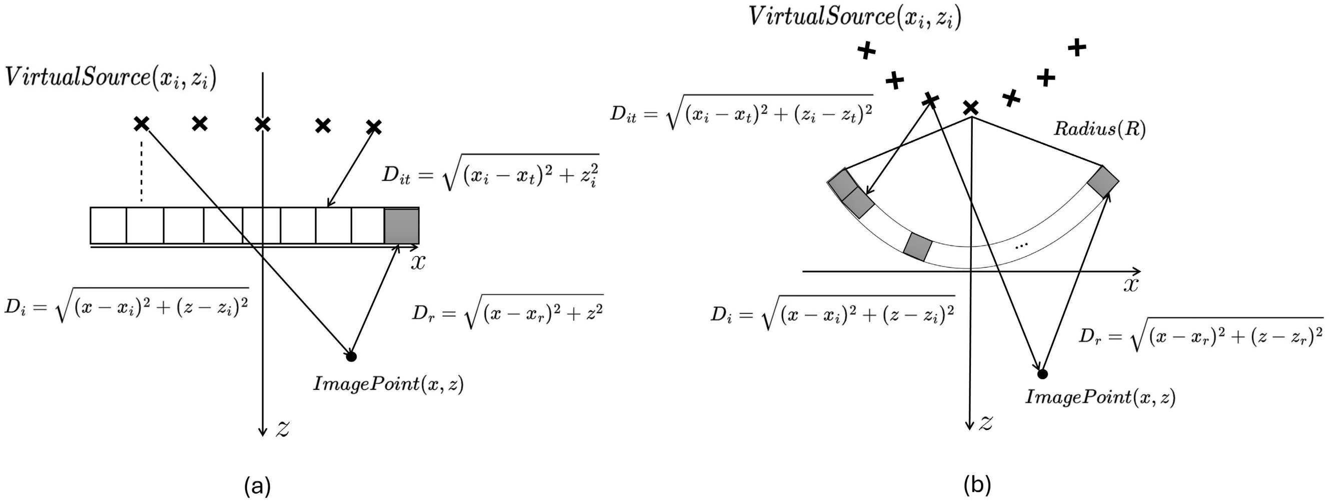

FIGURE 2. **Comparison of DW Linear and Convex Probe Configurations with distances between virtual source (x_i, z_i) and image point (x, z) and probe elements coordinates in transmission (x_t, z_t); moreover also the distance between image point and probe elements coordinates in reception (x_r, z_r) is displayed.**

to the image point and the sum of the distances between the virtual source and the probe element and between the probe element and the image point, all converted in time. By the triangular inequality, the difference can be zero only if the probe element is aligned along the line connecting the virtual source and the image point. Therefore, we computed the intersection point between the above line and the probe surface, for each virtual source position, thus obtaining the associated probe element and the corresponding apodization weight. For a convex probe of radius r_{probe}, the equation yielding the intersection points (x_e,z_e) is given by:

$$z_e = \frac{b}{m^2} + \frac{\sqrt{\left(\frac{b}{m^2}\right)^2 - \left(1+\frac{1}{m^2}\right)\left(\left(\frac{b}{m}\right)^2 - r_{probe}^2\right)}}{1+\frac{1}{m^2}} \tag{8}$$

$$x_e = \frac{z_e - b}{m} \tag{9}$$

where:

$$m = \frac{z - z_i}{x - x_i} \quad \text{and} \quad b = z - \left(\frac{z - z_i}{x - x_i}\right) \cdot x \tag{10}$$

Based on these intersection coordinates, the angle of intersection θ for a convex probe is calculated as follows:

$$\theta_e = \arctan\left(\frac{x_e}{z_e}\right) \tag{11}$$

For a linear probe, the x coordinate of the intersection point can be expressed as:

$$x_e = \left(-\frac{b}{m}\right) \tag{12}$$

The resulting intersection points are then used to map the transmit aperture onto the compound mask. Since the intersection point generally does not correspond to the center

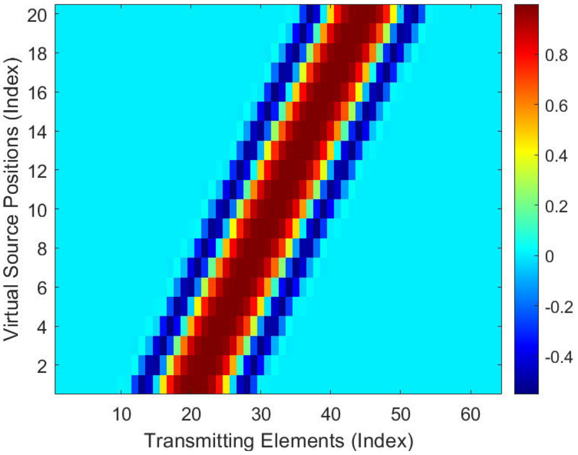

FIGURE 3. **Examples of values of $H(i, t)$ matrix in Eq. 7. Row and column indexes are related to virtual sources and probe elements indexes respectively.**

of a probe element, an interpolation across adjacent probe elements on apodization weights is carried out to compute the corresponding compound weight. In particular, for a linear geometry, defining $[x_t]$ the set of x coordinates of the transmit elements and $[v_t(x, z)]$ the corresponding set of transmit apodizations in SA for image point (x, y), the compound weight is computed as:

$$w_i(x, z) = interp([x_t], x_e, [v_t(x, z)]) \tag{13}$$

where $interp(a, b, c)$ if an interpolating function computing an off-grid value at coordinate b starting from a vector of values c a vector of on-grid coordinates a. A similar approach holds for convex geometries, where compound weights are computed as:

$$w_i(x, z) = interp([\theta_t], \theta_e, [v_t(x, z)]) \tag{14}$$

with $[\theta_t]$ being the set of angles related to transmit elements computed as in Eq. (11).

D. SA TRANSMIT APODIZATION COMPUTATION

As mentioned before, the compound mask computation starts from an arbitrary set of transmit apodizations $v_t(x, z)$ defined for SA imaging. A common choice, here adopted, for $v_t(x, z)$ to ensure image uniformity, is to start from a baseline apodization function $\hat{v}_t$ defined for a reference image point $(0, z_{ref})$ and compute the overall set $v_t(x, z)$ by interpolation of scaled and translated versions of $\hat{v}_t$. For linear geometries this can be done by:

$$v_t(x, z) = interp\left([x_t], \frac{(x_t - x)z_{ref}}{z}, [\hat{v}_t]\right) \tag{15}$$

For convex geometries the corresponding equation is:

$$v_t(x, z) = interp\left([\theta_t], \frac{(\theta_t - \theta)\rho_{ref}}{\rho}, [\hat{v}_t]\right) \tag{16}$$

where θ and ρ are the polar coordinates of image point (x, z) and ρ_{ref} is the radius polar coordinate corresponding to z_{ref} when $x = 0$. The baseline SA apodization $\hat{v}_t$ can be selected according to standard apodization windows like Hamming, Hann, Tukey, truncated Gaussian, each one with well known trade-off between main lobe width and side lobe height.

Algorithm 1 Compound Mask Computation for Divergent Wave Imaging for Linear and Convex Geometries

```
Input : Sets of probe elements coordinates[$(x_t, z_t)$], virtual
        sources coordinates [$(x_i, z_i)$], imaging grid coordinates
        [$(x, z)$], probe radius $r_{probe}$ (for convex probes )
Output: Set of compound mask weights [$w_i(x, z)$]
Define a baseline SA apodization $\hat{v}_t$ and a reference depth $z_{ref}$
for each imaging point $(x, z)$ do
    for each transmit element $t$ do
        // Compute SA transmit apodization
        if probe is convex then
            $v_t(x, z) = interp([\theta_t], \frac{(\theta_t-\theta)\rho_{ref}}{\rho}, [\hat{v}_t])$, Eq. 16
        if probe is linear then
            $v_t(x, z) = interp([x_t], \frac{(x_t-x)z_{ref}}{z}, [\hat{v}_t])$, Eq. 15
    for each virtual source $i$ do
        // compute intersection between
           probe ceramic and line
           connecting image point $(x, z)$ and
           virtual source $i$
        if probe is convex then
            Compute intersection angle $\theta_e$ by Eqs. 8-11
        if probe is linear then
            compute intersection coordinate $x_e$ by Eqs 10,12
        // Compute compound mask from
           interpolation of SA transmit
           apodization
        if probe is linear then
            $w_i(x, z) = interp([x_t], x_e, [v_t(x, z)])$ (Eq. 13)
        if probe is convex then
            $w_i(x, z) = interp([\theta_t], \theta_e, [v_t(x, z)])$ (Eq. 14)
return [$w_i(x, z)$]
```

E. ALGORITHM FOR COMPOUND MASK COMPUTATION

This section provides a structured overview and a pseudo-code for the algorithm used to derive the compound mask for DWI. The algorithm inputs are given by the probe geometry, the position of virtual sources and the imaging grid. There are two preliminary stages and a third stage that is the actual core of the algorithm:

Baseline Transmit Apodization Definition: The methodology begins by defining a baseline transmit apodization profile across the active probe elements $\hat{v}_t$. Standard apodization windows like Hamming, Hann etc. can be employed.

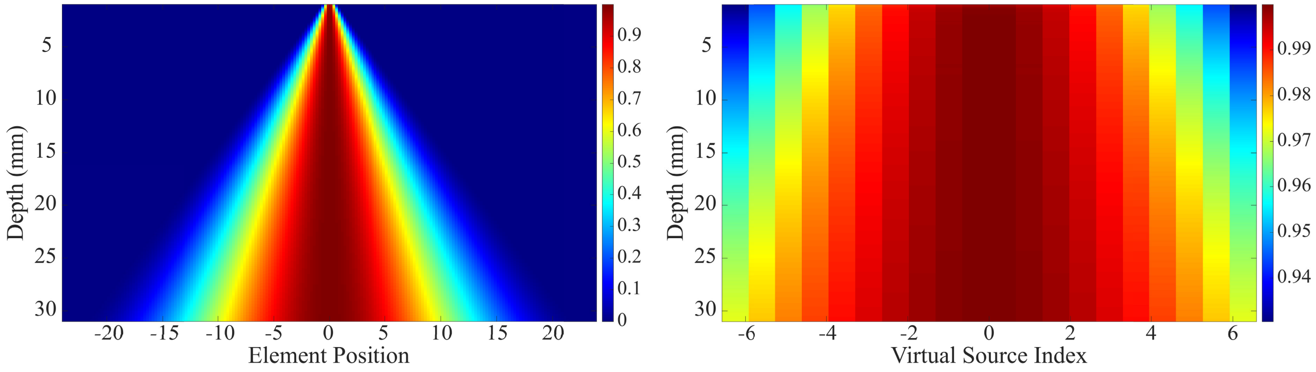

(a) (b)

FIGURE 4. Transmit apodization $v_t(x, z)$ in STAI, using Hanning window as baseline apodization. (a) and corresponding compound mask $w_i(x, z)$ in DWLA(b). Both maps are displayed for $x = 0$.

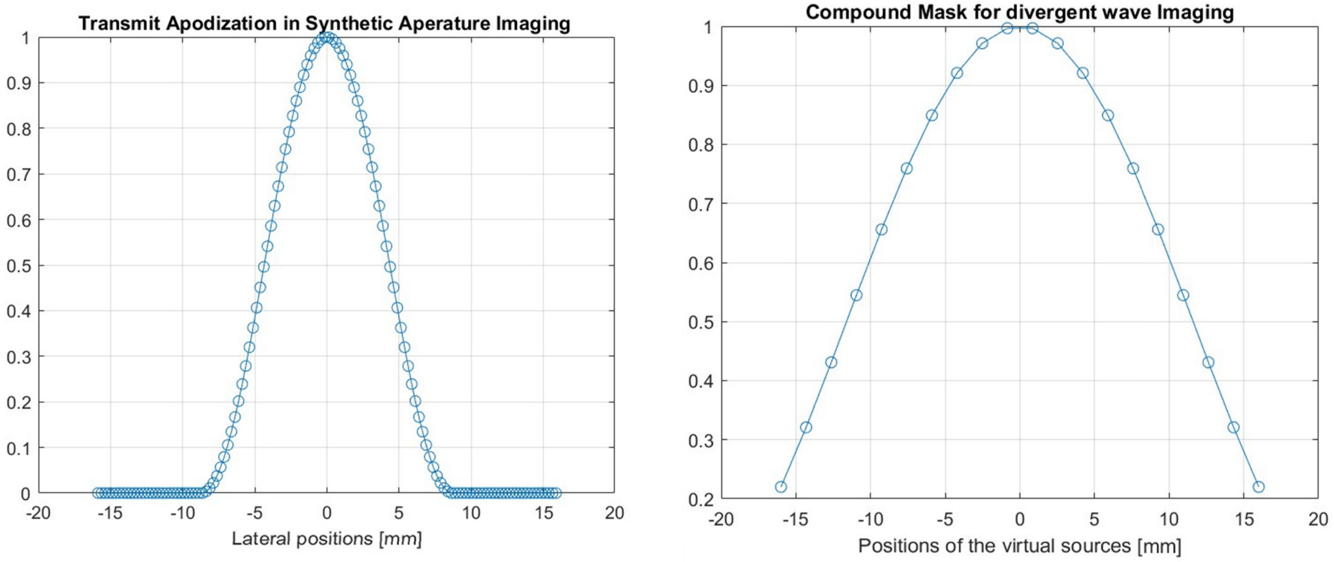

(a) (b)

FIGURE 5. (a) Transmit apodization $v_t(x, z)$ in STAI using Hanning window as baseline apodization with (b) The corresponding compound mask $w_i(x, z)$ in DWLA. Both plots are displayed for a fixed image point (x,z).

Apodization Mapping to Imaging Points: Since apodization window must adapt to varying depths and lateral positions, it gets a transformation based on the image point coordinates. This is achieved by interpolation of a translated and scaled version of the baseline apodization profile. The results is a set of apodization profiles $v_t(x, z)$, one for each image grid point (Eqs. 15-16).

Compound Mask Computation: In the final stage, for every combination of virtual source i and image point (x, y), a compound mask value $w_i(x, z)$ is computed from the apodization profile $v_t(x, z)$. The process involves two substeps. In the first one, the intersection between probe surface and line connecting image point (x, z) and virtual source point (x_i, z_i) is computed (Eqs. 8-12). In the second one, the value of apodization, associated to the probe surface location previously computed, is assigned to the compound mask value. Since the surface location is in general outside of the probe elements grid, an interpolation function is adopted (Eqs. 13,14).

The algorithm holds for both linear and convex geometries. What changes are the specific expressions for computing SA apodizations, intersections on probe surface and final interpolation to get the compound mask value.

F. SIMULATION SET-UP

The solution of the equations was validated through simulated data generated from the Field II software [24], [25]for both linear and convex probes. A 192-element array with a 5 MHz central frequency and 0.25 mm pitch was used for the linear probe, while a 3 MHz central frequency and 0.3 mm pitch were used for the convex probe with a radius of 50mm. A Hanning window was used in transmission and reception, with an F-number of 0.7 and 1.4 with a 2-cycle sinusoidal excitation signal. Pixel beamforming was performed on a grid of Z = 164 and X = 156. The image point spread function (PSF) for a point scatterer located at 20 mm and 30 mm depths was evaluated for the four cases, i.e. Synthetic Aperture Linear Array (SALA), Synthetic Aperture Convex Array (SACA), Divergent Wave Linear Array (DWLA), Divergent Wave Convex Array (DWCA). For DWLA a linear distribution of virtual sources placed at a fixed distance behind the probe surface has been adopted. This arrangement is depicted in Figure 2(a), where the virtual sources are evenly spaced along the x-axis directly behind the probe elements. For DWCA the virtual sources were positioned along a circle behind the probe surface (Figure 2(b)). Research on optimized virtual source distributions for linear probes and convex arrays in 2D imaging is limited. Therefore, a deterministic distribution of virtual sources is employed for both probe types according to the proposal detailed in [26]. For the linear probe, 20 virtual sources are uniformly distributed along the lateral axis, at a distance of 50 mm from the surface of the probe. These sources are positioned at regular intervals across a range of -25 to 25 times pitch. For the convex probe, the distribution of 20 virtual sources follows a curvilinear pattern to match the geometry of the probe elements. The angular range for these sources is defined by the maximum aperture angle set to 33°, covering a symmetric span on both sides of the probe's central axis. The curvilinear pattern of virtual sources is placed behind the probe, intersecting the probe center

G. EVALUATION METRIC

In ultrasound imaging, resolution is a critical measure of the ability to distinguish between two closely spaced objects. It is commonly divided into axial and lateral resolution. Axial resolution depends on the pulse length of the transmitted signal, while lateral resolution is influenced by beam focusing and aperture size. The Full Width at Half Maximum (FWHM) is a widely used metric to evaluate lateral resolution. The FWHM quantifies the beamwidth of the Point Spread Function (PSF) at the point where its intensity drops to −6 dB from its peak. This corresponds to half the maximum intensity ($I_{\max}$), since:

$$20\log_{10}\left(\frac{I}{I_{\max}}\right) = -6\,\text{dB} \quad \Rightarrow \quad I = \frac{I_{\max}}{2}.$$

Mathematically, for a PSF intensity function $I(x)$,the FWHM is defined as the difference between two lateral positions x_1 and x_2 where the intensity reaches half of its peak:

$$I(x_1) = I(x_2) = \frac{I_{\max}}{2}, \quad \text{FWHM} = |x_2 - x_1|. \tag{17}$$

The PSF describes how energy is distributed in the imaging field from a point scatterer. A smaller FWHM indicates better lateral resolution, allowing for more precise differentiation between closely spaced scatterers [24].

III. RESULTS

Figure 4 shows how the transmit apodization weights are transformed into the compound mask, the apodization weights function of probe position (left) and the compound mask function of virtual source index are displayed for a set of image points depths (i.e. the y coordinate of the displayed images), for the linear probe case. As it can be seen the transformation consists in a geometric warping that locally preserves the numerical values. Figure 5 also illustrates the relationship between the transmit apodization used in synthetic aperture imaging (STAI) and the corresponding compound mask applied for divergent wave imaging (DWI), for a fixed image point. The left plot represents the transmit apodization applied to the lateral positions of the transducer elements during STAI. This apodization function demonstrates a smooth distribution of weights, peaking at the center and tapering off towards the edges, ensuring optimal energy distribution during transmission. The right plot depicts the derived compound mask for DWI, showing the corresponding weights as a function lateral position of the virtual sources (the virtual source depth is assumed to be fixed in this example). The derived mask closely mirrors the behavior of the STAI apodization but is adjusted for the spatial distribution of the virtual sources.

The images of point-like scatterers are displayed in Figure 6 and Figure 7 using F-number 0.7 and F-number of 1.4 respectively and their evaluation in terms of full width at half maximum (FWHM) is reported in Table2 and table3. For linear probes, the Full Width at Half-Maximum (FWHM) with DWLA increased by 7.5% at 20 mm and by 9% at 30 mm compared to SALA. In contrast, DWCA showed a much smaller increase of 1.64% at 20 mm and a substantial increase of 26.56% at 30 mm compared to SACA, with a slight increase in sidelobes. Overall the proposed approach for the computation of the compound mask seems to reproduce quite accurately the effect of transmit apodization in Synthetic Aperture in terms of spatial resolution, except for the case of DWCA at 30 mm. This result accounts for the fact that the spatial distribution of virtual sources also plays a crucial role in image optimization, and it may limit the accuracy of mapping between STAI apodization and DWCA compounding. These aspects will be investigated in future studies. Concerning the side-lobe level, the worsening is likely due to the non-ideal nature of the divergent wavefield, given by the boundary effect introduced by the finite aperture.

IV. DISCUSSION

This study presents a novel approach for computing compound mask weights in Divergent Wave Imaging (DWI) using

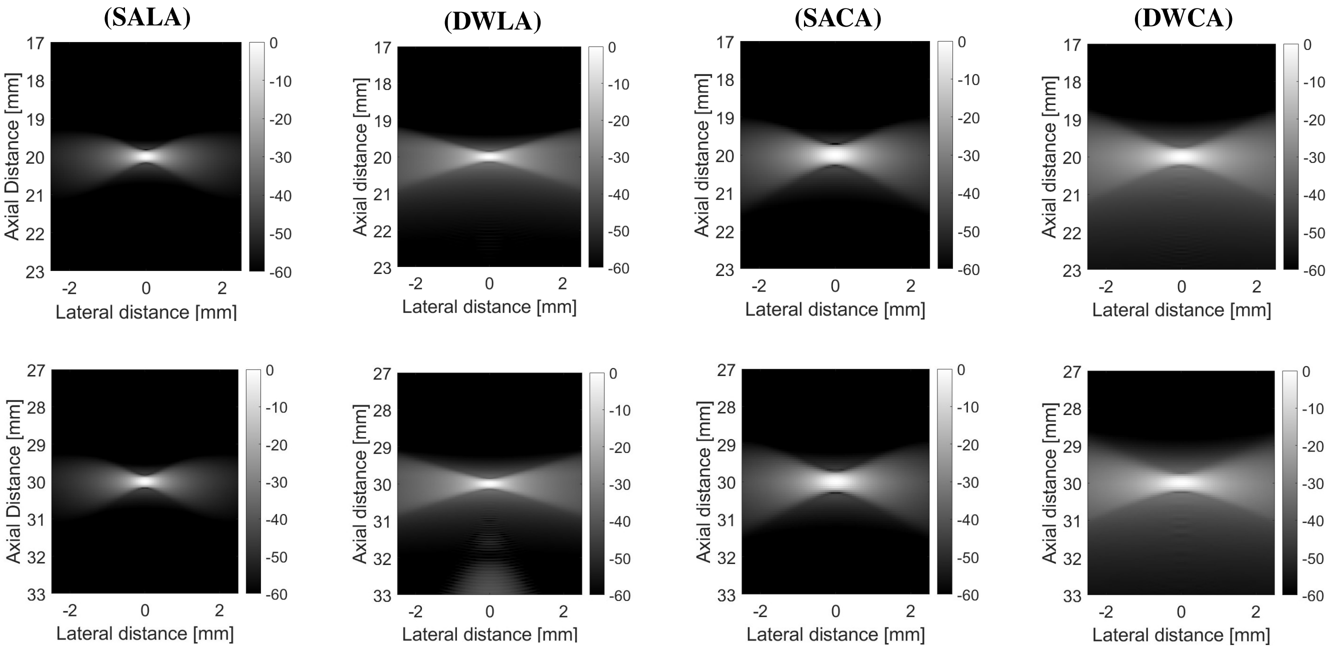

FIGURE 6. PSF of SALA, DWLA, SACA, and DWCA for a point at 20 mm depth (first row), and 30mm depth (second row) with F-number=0.7.

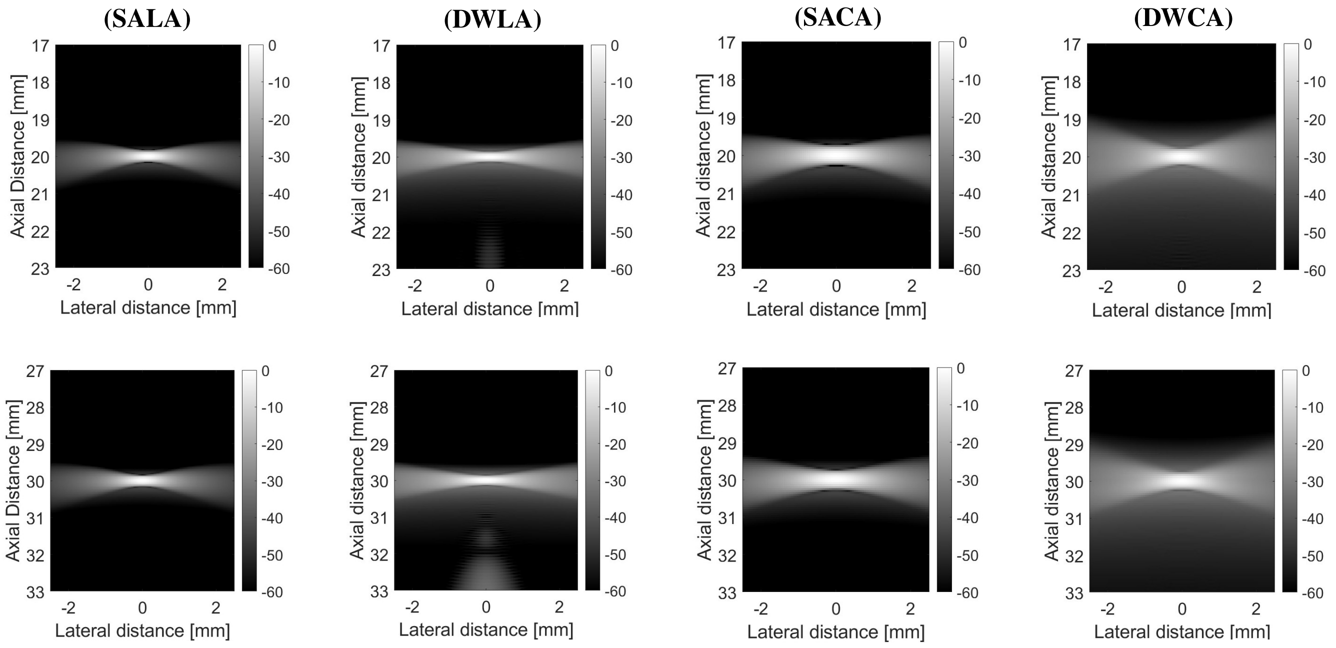

FIGURE 7. PSF of SALA, DWLA, SACA, and DWCA for a point at 20 mm depth (first row), and 30mm depth (second row) with F-number 1.4.

a closed-form mapping from Synthetic Aperture Imaging (SAI) transmit apodization weights. Unlike traditional trial-and-error-based weighting methods, the proposed approach enables a direct, systematic computation of optimal weights, thereby improving spatial resolution. The results demonstrate that the method effectively maintains the apodization profile in DWI, achieving a minimal loss in resolution compared to SAI, as evidenced by the FWHM described in section II-E analysis across different probe configurations. Building upon previous studies that explored the relationship between coherent plane-wave compounding (CPWC) and SAI [18] for optimizing apodization strategies, this work extends those principles specifically to DWI using a systematic mapping function. By leveraging a closed-form transformation,

TABLE 2. **Comparison of FWHM values at 20 mm and 30 mm for different techniques with F-number 0.7.**

Technique	FWHM at 20 mm	FWHM at 30 mm
SALA	0.40	0.43
DWLA	0.43	0.47
SACA	0.61	0.64
DWCA	0.62	0.81

TABLE 3. **Comparison of FWHM values at 20 mm and 30 mm for different techniques with F-number 1.4.**

Technique	FWHM at 20 mm	FWHM at 30 mm
SALA	0.65	0.68
DWLA	0.8	0.95
SACA	0.8	0.84
DWCA	0.88	1

the proposed approach eliminates the need for computationally expensive adaptive beamforming [15] or iterative weight estimation techniques [19], allowing for a pre-computed derived compound mask applicable to both linear and convex probe geometries. This advancement leads to several key benefits, including a significant reduction in computational burden since the compound mask weights can be computed offline, making the method highly suitable for high-frame-rate imaging applications. Furthermore, its ability to adapt seamlessly to different probe geometries ensures broad applicability across diverse ultrasound imaging setups. The findings also indicate that the proposed method successfully preserves spatial resolution, as demonstrated by the minimal FWHM degradation observed in linear and convex array configurations at different depths (table2, table3). This methodological advancement is particularly valuable for medical ultrasound diagnostics, where high-frame-rate imaging is critical for applications such as cardiac and abdominal imaging [27], [28]. Ultimately, this work introduces an innovative signal-processing framework for DWI, bridging the gap between theoretical apodization formulations and practical implementation. By ensuring computational efficiency, preserving spatial resolution, and offering applicability across multiple imaging configurations.

V. LIMITATIONS AND POTENTIAL IMPROVEMENTS

This study primarily relies on simulations conducted using Field II software, but simulations alone cannot fully account for the complexities encountered in real-world scenarios, such as tissue heterogeneity. Therefore, experimental validation through in vitro or in vivo testing is necessary to comprehensively evaluate the effectiveness of our proposed method. Nevertheless, Field II has been extensively validated and is widely used within the ultrasound imaging community due to its accuracy in simulating wave propagation and evaluating imaging techniques. Moreover, numerous studies have shown that simulation-based results often correlate with in vivo findings for similar imaging methods [22], [29], Another limitation of this study is that the proposed compound mask approach is designed to operate with transmit signals that are short in time domain. While this constraint simplifies the transformation and ensures accurate mapping of synthetic aperture imaging (SAI) transmit apodization weights to divergent wave imaging (DWI), it may limit the generalizability of the method to imaging setups or applications where longer transmit pulses are required. Also, the current approach does not explicitly account for the contribution of nearby elements when calculating the compound mask weights as a function of the apodization of a single probe element. Neighboring elements may have a significant impact on the transmitted and received signals.

One of the notable strengths of this study is the computation of optimized weights without the need for complex optimization algorithms, achieved by leveraging a closed-form approach. This method offers a streamlined solution that eliminates the necessity of iterative optimization processes, reducing computational overhead. Furthermore, the proposed approach introduces no additional computational load to divergent wave imaging (DWI). The compound mask weights can be efficiently computed offline and stored in memory, as demonstrated in [23], thereby minimizing the need for real-time computations and ensuring a resource-efficient implementation. Additionally, this study extends the application of the compound mask method beyond linear geometries by introducing its use for convex array configurations. This expansion represents a significant step forward in making the method applicable to a broader range of imaging scenarios, offering versatility and adaptability in high-frame-rate ultrasound imaging. Moreover, the presented mapping approach has the potential to be utilized in future research to optimize other imaging parameters, such as the distribution of virtual sources. By identifying optimal virtual source arrangements, it is possible to further enhance image quality and performance across various divergent wave imaging setups.

VI. CONCLUSION

This study has demonstrated an approach to applying a compound mask in divergent wave imaging (DWI) by deriving a transformation from synthetic aperture imaging (SAI). The derived transformation enables using the same apodization window in synthetic transmit aperture imaging (STAI) for divergent waves (DW), effectively linking the compound mask with transmit apodization for each virtual source position. The results from simulated data using linear and convex probes validate the theoretical derivations. By examining the point spread function (PSF) at two different depths and comparing the full width at half-maximum (FWHM), it was found that the transformed apodization accurately replicates the effect of the STAI transmit apodization The results from simulated data confirm that the proposed compound mask method preserves the effect of transmit apodization in Synthetic Aperture Imaging

(SAI) for divergent waves, as evidenced by a 7.5% and 9% increase in Full Width at Half Maximum (FWHM) at depths of 20 mm and 30 mm, respectively, for the Divergent Wave Linear Array (DWLA) compared to the Synthetic Aperture Linear Array (SALA). Similarly, for the Divergent Wave Convex Array (DWCA), a smaller increase of 1.64% at 20 mm and a more pronounced increase of 26.56% at 30 mm compared to the Synthetic Aperture Convex Array (SACA) was observed. These results highlight the ability of the proposed method to accurately replicate transmit apodization effects while optimizing compound mask weights in both linear and convex geometries.

Future research will focus on several key areas to extend and enhance the proposed approach. First, experimental validation using clinical datasets using linear and convex probe and the available open-source ultrasound machine (e.g.,ULA-OP, Verasonic..) will be performed on tissue-mimicking multi-purpose phantom to assess the practical applicability and robustness of the compound mask method in real-world scenarios. Further optimization of divergent wave imaging parameters, such as virtual source positions, will be explored. By leveraging the mapping criteria developed in this study, we aim to identify parameters that can predict optimal virtual source distributions without generating point spread function (PSF) plots. This will enable a more intuitive and computationally efficient approach to position determination, potentially reducing trial-and-error in imaging setups. Another important area for future exploration is the adaptation and refinement of the compound mask technique for more complex imaging geometries, including 3D imaging configurations. Expanding the approach to three-dimensional probes could unlock new applications and improve image quality and resolution.

REFERENCES

[1] H. Hasegawa and H. Kanai, "High-frame-rate echocardiography using diverging transmit beams and parallel receive beamforming," *J. Med. Ultrason.*, vol. 38, no. 3, pp. 129–140, Jul. 2011, doi: 10.1007/s10396-011-0304-0.

[2] J. Porée, D. Posada, A. Hodzic, F. Tournoux, G. Cloutier, and D. Garcia, "High-frame-rate echocardiography using coherent compounding with Doppler-based motion-compensation," *IEEE Trans. Med. Imag.*, vol. 35, no. 7, pp. 1647–1657, Jul. 2016, doi: 10.1109/TMI.2016.2523346.

[3] T. L. Szabo and P. A. Lewin, "Ultrasound transducer selection in clinical imaging practice," *J. Ultrasound Med.*, vol. 32, no. 4, pp. 573–582, Apr. 2013.

[4] P. Song, A. Manduca, J. D. Trzasko, and S. Chen, "Ultrasound small vessel imaging with block-wise adaptive local clutter filtering," *IEEE Trans. Med. Imag.*, vol. 36, no. 1, pp. 251–262, Jan. 2017.

[5] D. Maresca, M. Correia, O. Villemain, A. Bizé, L. Sambin, M. Tanter, B. Ghaleh, and M. Pernot, "Noninvasive imaging of the coronary vasculature using ultrafast ultrasound," *J. Amer. Coll. Cardiol. Imag.*, vol. 11, no. 6, pp. 798–808, 2018.

[6] G. Montaldo, M. Tanter, J. Bercoff, N. Benech, and M. Fink, "Coherent plane-wave compounding for very high frame rate ultrasonography and transient elastography," *IEEE Trans. Ultrason., Ferroelectr., Freq. Control*, vol. 56, no. 3, pp. 489–506, Mar. 2009, doi: 10.1109/TUFFC.2009.1067.

[7] P. J. Thoen, "Aperture apodization to reduce the off-axis intensity of the pulsed-mode directivity function of linear arrays," *Ultrasonics*, vol. 20, no. 5, pp. 231–236, 1982.

[8] C. M. W. Daft and W. E. Engeler, "Windowing of wide-band ultrasound transducers," in *Proc. IEEE Ultrason. Symp.*, vol. 2, Jul. 1996, pp. 1541–1544.

[9] K. E. Thomenius, "Evolution of ultrasound beamformers," in *Proc. IEEE Ultrason. Symp.*, vol. 2, Jan. 1996, pp. 1615–1622.

[10] D. A. Guenther and W. F. Walker, "Optimal apodization design for medical ultrasound using constrained least squares Part II simulation results," *IEEE Trans. Ultrason., Ferroelectr., Freq. Control*, vol. 54, no. 2, pp. 343–358, Feb. 2007.

[11] S. Repetto and A. Trucco, "A stochastic approach for the apodization of very short arrays," *Ultrasonics*, vol. 42, nos. 1–9, pp. 425–429, Apr. 2004.

[12] S. M. Sakhaei, A. Mahloojifar, and H. Ghassemian, "A transformation based method to design ultrasound array," *Ultrasonics*, vol. 49, no. 2, pp. 179–184, 2009.

[13] J. F. Synnevag, A. Austeng, and S. Holm, "Adaptive beamforming applied to medical ultrasound imaging," *IEEE Trans. Ultrason., Ferroelectr., Freq. Control*, vol. 54, no. 8, pp. 1606–1613, Aug. 2007.

[14] C. Seo and J. Yen, "Sidelobe suppression in ultrasound imaging using dual apodization with cross-correlation," *IEEE Trans. Ultrason., Ferroelectr., Freq. Control*, vol. 55, no. 10, pp. 2198–2210, Oct. 2008, doi: 10.1109/TUFFC.919.

[15] J.-F. Synnevåg, A. Austeng, and S. Holm, "A low-complexity data-dependent beamformer," *IEEE Trans. Ultrason., Ferroelectr., Freq. Control*, vol. 58, no. 2, pp. 281–289, Feb. 2011.

[16] J. A. Jensen, S. I. Nikolov, K. L. Gammelmark, and M. H. Pedersen, "Synthetic aperture ultrasound imaging," *Ultrasonics*, vol. 44, pp. e5–e15, Dec. 2006.

[17] L. Sandrin, S. Catheline, M. Tanter, X. Hennequin, and M. Fink, "Time-resolved pulsed elastography with ultrafast ultrasonic imaging," *Ultrason. Imag.*, vol. 21, no. 4, pp. 259–272, Oct. 1999.

[18] A. Rodriguez-Molares, H. Torp, B. Denarie, and L. Løvstakken, "The angular apodization in coherent plane-wave compounding [correspondence]," *IEEE Trans. Ultrason., Ferroelectr., Freq. Control*, vol. 62, no. 11, pp. 2018–2023, Nov. 2015.

[19] O. M. H. Rindal and A. Austeng, "Double adaptive plane-wave imaging," in *Proc. IEEE Int. Ultrason. Symp. (IUS)*, Tours, France, Sep. 2016, pp. 1–4.

[20] S. Goudarzi, A. Asif, and H. Rivaz, "Angular apodization estimation using independent component analysis in coherent plane-wave compounding," *IEEE Trans. Ultrason., Ferroelectr., Freq. Control*, vol. 67, no. 5, pp. 989–998, May 2020, doi: 10.1109/TUFFC.2020.2971892.

[21] V. Komini, P. Santos, and J. D'Hooge, "Diverging wave compounding: Direct comparison of two popular approaches," in *Proc. IEEE Int. Ultrason. Symp. (IUS)*, Washington, DC, USA, Sep. 2017, pp. 1–4, doi: 10.1109/ULTSYM.2017.8092802.

[22] C. Papadacci, M. Pernot, M. Couade, M. Fink, and M. Tanter, "High-contrast ultrafast imaging of the heart," *IEEE Trans. Ultrason., Ferroelectr., Freq. Control*, vol. 61, no. 2, pp. 288–301, Feb. 2014.

[23] Z. Alzein, M. Crocco, and D. D. Caviglia, "Computationally efficient RF band and base band beam-former for coherent plane wave imaging," in *Proc. 19th Conf. Ph.D Res. Microelectron. Electron. (PRIME)*, Larnaca, Cyprus, Jun. 2024, pp. 1–4, doi: 10.1109/PRIME61930.2024.10559667.

[24] J. A. Jensen, "FIELD: A program for simulating ultrasound systems," *Med. Biol. Eng. Comput.*, vol. 34. no. 1, pp. 351–353, Mar. 1996.

[25] J. A. Jensen and N. B. Svendsen, "Calculation of pressure fields from arbitrarily shaped, apodized, and excited ultrasound transducers," *IEEE Trans. Ultrason., Ferroelectr., Freq. Control*, vol. 39, no. 2, pp. 262–267, Mar. 1992.

[26] S. Liang and L. Wang, "A study of wide unfocused wavefront for convex-array ultrasound imaging," *Ultrasonics*, vol. 134, Sep. 2023, Art. no. 107080, doi: 10.1016/j.ultras.2023.107080.

[27] J. Grondin, V. Sayseng, and E. E. Konofagou, "Cardiac strain imaging with coherent compounding of diverging waves," *IEEE Trans. Ultrason., Ferroelectr., Freq. Control*, vol. 64, no. 8, pp. 1212–1222, Aug. 2017, doi: 10.1109/TUFFC.2017.2717792.

[28] M. Cikes, L. Tong, G. R. Sutherland, and J. D'Hooge, "Ultrafast cardiac ultrasound imaging," *JACC, Cardiovascular Imag.*, vol. 7, no. 8, pp. 812–823, Aug. 2014, doi: 10.1016/j.jcmg.2014.06.004.

[29] Y. Chen, Z. Zhuang, J. Luo, and X. Luó, "Doppler and pair-wise optical flow constrained 3D motion compensation for 3D ultrasound imaging," *IEEE Trans. Image Process.*, vol. 32, pp. 4501–4516, 2023.

ZAHRAA ALZEIN was born in Lebanon. She received the bachelor's degree in electronics and the master's degree in signal, image processing, and telecommunications from Lebanese University, Beirut, Lebanon, in 2018 and 2020, respectively. She is currently pursuing the Ph.D. degree in electrical engineering with the University of Genoa, Genoa, Italy, in collaboration with Esaote Company, focusing on advanced ultrasound imaging techniques. She has involved on various projects during her studies, including the optimization of ultrasound beamforming techniques. Her current research interests include focused transmit ultrasound systems and ultrafast imaging. She has been actively involved in IEEE conferences. She received recognition for her work on computationally efficient ultrasound beamforming and continues to contribute to the advancement of medical ultrasound imaging technology.

MARCO CROCCO received the Laurea degree in electronic engineering and the Ph.D. degree in electronic engineering, computer science and telecommunications from the University of Genoa, Genoa, Italy, in 2005 and 2009, respectively. From 2005 to 2010, he was with the Department of Biophysical and Electronic Engineering, University of Genoa. From 2010 to 2015, he joined as a Post-Doctoral Fellow with the Pattern Analysis and Computer Vision Department and the Visual Geometry and Modeling Laboratory, Istituto Italiano di Tecnologia, Genoa. He is currently working on signal processing applied to medical ultrasound with Esaote S.p.A.

DANIELE D. CAVIGLIA (Life Member, IEEE) is currently a Full Professor of electronics with the Department of Electrical, Electronics and Telecommunications Engineering and Naval Architecture (DITEN), University of Genoa, Italy, where he teaches courses of electronic systems for telecommunications with the Laboratory of Electronics and Embedded Systems. His current research interests include the design of electronic circuits and systems for telecommunications, electronic equipment for health and safety, and energy harvesting techniques for the Internet of Things (IoT) applications. He is also active in the development of innovative solutions for environmental monitoring and this activity led to the foundation of Artys s.r.l., as a spin-off of the University of Genoa, in 2014.

• • •